Springer

Acta Mechanica Sinica

CrossMark click for updates

• RESEARCH PAPER •

Acta Mech. Sin., Vol. 40, 323233 (2024)
https://doi.org/10.1007/s10409-023-23233-x

Reconstruction of the internal volume fraction for particle-liquid system from imaging indicators by refractive index matching

Yunhui Sun[1], Jiajun Jiao[1], Yi An[2], Xiaoliang Wang[1*], and Qingquan Liu[1]

[1] *School of Aerospace Engineering, Beijing Institute of Technology, Beijing 100081, China;*
[2] *Key Laboratory for Mechanics in Fluid Solid Coupling Systems, Institute of Mechanics, Chinese Academy of Sciences, Beijing 100190, China*

Received May 19, 2023; accepted August 17, 2023; published online January 31, 2024

Refractive index matching (RIM) is widely used to investigate particle-liquid mixture flows. However, determining the volume fraction ϕ in RIM is generally empirical and lacks theoretical or experimental basis. To reasonably reconstruct the internal ϕ, this study performs systematic calibration experiments to study the relationship between ϕ and the imaging indicators. The results show that the model based on area fraction c_{2D} will induce a large error for low ϕ owing to the instability of the particle's apparent size. The traditionally adopted proportional function $\phi = ac_{2D}$ is only valid for ϕ near the calibration point. A predictive model is proposed based on the size of the Voronoi cell, d_{poly}, which proves to be more accurate and stable in RIM experiments. The d_{poly}-based model is applied to dense granular flows down an inclined plane to study the internal profiles of ϕ and the bottom normal stress.

Refractive index matching, Volume fraction, Area fraction, Voronoi diagram, Inclined flow

Citation: Y. Sun, J. Jiao, Y. An, X. Wang, and Q Liu, Reconstruction of the internal volume fraction for particle-liquid system from imaging indicators by refractive index matching, Acta Mech. Sin. **40**, 323233 (2024), https:// doi.org/10.1007/s10409-023-23233-x

1. Introduction

Particle-liquid mixtures are common in natural environmental and industrial processes. Typical examples are large-scale natural disasters such as landslides and debris flows, sediment transport that alters riverbed morphology and flows in industrial equipment such as dense cyclones and fluidized beds [1, 2]. Current research on granular flow is far from complete, especially on the constitutive relations for granular stress [3-5].

For a typical two-phase flow, the solid volume fraction ϕ (or packing density) is an important parameter that describes the packing or flowing behavior of the granular materials. It is defined as the proportion of the solid volume to total volume (solids + liquids), i.e., $\phi = V_{solid}/(V_{solid} + V_{liquid})$, where V_{solid} and V_{liquid} denote solid and liquid volumes, respectively. The constitutive relations generally relate the stresses with ϕ and other parameters describing the flow state, such as shear rate and granular temperature [4, 6-8]. Though the stress is difficult to be directly measured, for several steady flows such as granular flow down an inclined plane [9], annular shear [10], and sediment transport [11, 12], the tangential or normal stress balances the corresponding component of gravity, and its measurement is ultimately reduced to integrating the volume fraction over the depth. Besides, the granular material is known to dilate or compact when sheared, mainly depending on the packing state [13], which presents to be an important physics influencing the granular flow. This phenomenon is widely described by dilatancy models which relate the dilation or compaction rate with the deviation of the current solid volume fraction from the steady state [14-16]. Therefore, accurately measuring the volume fraction is essential to investigate particle-liquid flows, thereby benefiting developments of more reliable constitutive relations and two-phase models.

*Corresponding author. E-mail address: wangxiaoliang36@bit.edu.cn, wangxiaoliang52086@126.com (Xiaoliang Wang)
Executive Editor: Huan Zhang

The traditional methods of measuring volume fraction can be generally categorized into two types: direct measurement and imaging methods. The simplest way to directly measure ϕ is to measure the volume of the solid phase in the samples and calculate ϕ following its definition [9, 17]. However, the sampling operation can be quite troublesome and may influence the flow. More importantly, the result is actually a bulk volume fraction and can be seen as an average value of ϕ. For cases when the flow is highly heterogeneous and the local volume fraction in some specific area is needed, this simple but probably the most accurate way loses its effectiveness. Researchers therefore use real-time, local and non-intrusive methods such as those using electrical capacitance technique [18], radiation attenuation techniques based on the γ-ray or X-ray [19, 20] and acoustics technique [21]. A more widely adopted approach is the imaging method that uses the image features as indicators to derive the volume fraction. For granular flow near a wall, Capart et al. [22] constructed the Voronoi diagram based on the recognized granular center and related the geometric parameters of the Voronoi cells with the volume fraction. This technique was further extended to a stereoscopic application [23]. A transverse laser sheet was introduced by Spinewine et al. [24] to illuminate near-wall particles, and the granular-averaged distance from the wall was acquired, which was converted to the volume fraction [25]. Sarno et al. [26] proposed a binarization algorithm to obtain the two-dimensional (2D) area fraction of the solid phase and found its exponential relationship with the actual three-dimensional (3D) volume fraction.

The aforementioned imaging methods can only derive the near-wall volume fraction based on imaging indicators. In fact, traditional experiments are limited by the natural opacity of the granular materials and can only obtain near-wall or near-free-surface flow information. In contrast, refractive index matching (RIM) provides a relatively simple and inexpensive tomographic technique to directly acquire the inner packing or flow information, which represents a true state unaffected by the wall [27-29]. RIM has been widely used in many investigations such as on granular material [10, 30, 31] and interstitial flows in porous media [32, 33]. Ideally, RIM scanning can be used to reconstruct the 3D position and size of the particles and derive the volume fraction. However, the scanning device and reconstruction technique are typically complex and not easily used especially in the case of a fast flow. A fixed laser is widely adopted whereby only particles intersecting the laser sheet are observed. The volume fraction is traditionally believed to be proportional to the 2D area fraction c_{2D}, i.e., $\phi = ac_{2D}$, and the coefficient a is obtained from c_{2D} of a dense packing state (if it exists) whose volume fraction is assumed to be $\phi_0 = 0.58$. However, this method is questionable because ϕ_0 is not usually confirmed and the proportional relation itself lacks theoretical or experimental basis.

It is seen that determining solid volume fraction is still subject to a high degree of uncertainty in experimental investigations of granular flows. In particular, the RIM technique, which is promising for obtaining more reasonable information at greater depth inside a granular flow, has to determine the volume fraction empirically. This study aims to develop a reliable imaging method to measure the solid volume fraction in RIM experiments. The factors affecting the imaging characteristics are discussed in Sect. 2. The calibration experiment and analysis methodology are introduced in Sect. 3. Section 4 focuses on the variations in image characteristics under different volume fractions, systematically compares the indicators and corresponding models for predicting volume fraction and proposes a new model based on the Voronoi diagram. The proposed model is applied to a real case in Sect. 5. The conclusions and further possible improvements are given in Sect. 6.

2. RIM imaging characteristics

The basic idea of RIM is matching the refractive indexes (RIs) of both particles and liquid to obtain a nearly transparent mixture, which is also called transparent soil [34]. The inner particles are visualized with the help of plane laser-induced fluorescence (PLIF) technique. This section analyzes the particle imaging characteristics and influencing factors.

2.1 Refractive index mismatch

RIM experiments require close matching between the RIs of the two phases. Dijksman et al. [27] argued that the RI mismatch should be less than ± 0.003 to achieve acceptable imaging quality for a depth of 15 particle layers. However, mismatching is unavoidable owing to the following reasons:

(1) The RI changes with temperature, and the RI of the liquid phase typically changes more than that of the solid phase. Taking the dimethyl sulfoxide (DMSO) used in this study as an example, the changing rate reaches 0.0005/K [35], which may result in significant RI deviation unless the temperature is strictly controlled.

(2) Even for the same batch of particles, the RI may vary up to 0.01 owing to the material non-uniformity or impurities during manufacture [27, 29]. These abnormal particles are difficult to exclude and may result in stripes when intersecting the laser sheet.

(3) The RI itself depends on the wavelength especially for the liquid phase. Fluorescence is usually introduced to

enhance contrast between the two phases. The wavelength of fluorescence is longer than that of the laser owing to the Stokes shift. If the RIs are matched at the fluorescence excitation wavelength, the mismatch is significant along the laser path where fluorescence dominates. While matching RIs at the fluorescence emission wavelength causes significant mismatch in the mixture, which may cause imaging distortion [36].

As a result, laser refraction occurs at the solid-liquid interface, which distorts the laser sheet. Furthermore, certain scratches exist on the particle surfaces that cause diffuse reflection of the laser, especially after long use of the granular materials. The refraction and diffuse reflection result in significant laser sheet distortion and intensity attenuation. The degree of distortion or intensity attenuation is often used as an indicator of the effectiveness of RIM, while even perfect matching has shown a certain distortion or attenuation [28]. The laser distortion, which tends to be more severe at greater depth along the laser path, may introduce to the image the particle portions lying outside of the expected object plane. Generally, the maximum number of layers the laser can penetrate into the transparent soil without significant distortion, l_s, is limited, and the maximum number of layers the fluorescence traverses the mixture to the camera, l_f, is also limited. Their sum is typically assumed to be constant at approximately 30 for a good RIM state [27].

2.2 Laser

The laser traditionally used is a Gaussian beam, which is transformed into a radial laser sheet by a Powell or cylindrical lens. The laser sheet thickness H is related to the original laser beam diameter. The laser sheet is thicker at increasing distance from the beam waist. Considering also the aforementioned laser distortion, H is thus inconsistent in the region of interest (ROI). Additionally, the laser intensity varies along the path as $I \propto 1/r$ because of the radial transmission. The intensity further decreases owing to fluorescence absorption. To summarize, as an important tool for visualizing internal particles, the laser sheet suffers from significant variations in both geometry (thickness) and intensity, which need to be taken into account when using the geometric properties or image brightness to determine the volume fraction.

2.2.1 *Influence of the laser sheet thickness*

Assuming that the solid phase is composed of ideal spherical particles with radius R, the projection of the illuminated portion of the particle by the laser sheet is a circle with apparent radius r. Since the thickness H of the laser sheet is non-zero, the particle is overprojected, which is also called the Holmes effect [37]. The apparent radius r is the maximum radius of each section of the illuminated portion as shown in Fig. 1(a) and (b). When the laser crosses the middle section, one has $r = R$. It is further assumed that the position x of the laser relative to the particle center is random and the particle positions are uncorrelated. The relationship between r and x is shown in Fig. 1(c). The cumulative distribution function (CDF) of r is given by

$$F(r) = \begin{cases} 2\left[R - x(r)\right]/(2R + H), & r < R, \\ 2R/(2R + H), & r = R^-, \\ 1, & r = R, \end{cases} \tag{1}$$

where $x(r) = \sqrt{R^2 - r^2}$. The probability of a full-sized projection is $P(r = R) = H/(2R + H)$. It is seen that the CDF is related to both the particle size R and laser thickness H, and there is an abrupt change when r tends to R. The probability density function (PDF) of r is

$$f(r) = \frac{\mathrm{d}F(r)}{\mathrm{d}r} = \frac{2r}{(2R + H)x(r)} \quad \text{for} \quad r < R. \tag{2}$$

The probability for $r_1 \le r \le r_2$ is

$$\begin{aligned} P(r_1 \le r \le r_2) &= F(r_2) - F(r_1) \\ &= \begin{cases} 2\left[x(r_1) - x(r_2)\right]/(2R + H), & r_2 < R, \\ \left[2x(r_1) + H\right]/(2R + H), & r_2 = R, \end{cases} \end{aligned} \tag{3}$$

which is shown in Fig. 1(d). For $r < R$, the occurrence probability increases monotonically as r increases. The probability of a full-sized projection increases and the probability of smaller-sized projections decreases when the laser becomes thicker. This implies that the apparent size tends to enlarge especially when H is not negligible compared to R.

Based on the PDF of r, the averaged projection area of the particle is

$$\bar{A} = \int_0^{R^-} f(r)\pi r^2 \mathrm{d}r + \frac{\pi H R^2}{2R + H} = \frac{4 + 3H/R}{6 + 3H/R}\pi R^2. \tag{4}$$

In our experiments, the laser thickness varies as $H/R \in [0.5, 0.8]$ without considering the laser distortion (see Sect. 3.1). The result gives $\bar{A}|_{H/R=0.8} \approx 1.04\bar{A}|_{H/R=0.5}$, i.e., the averaged area expands by approximately 4%. Therefore, when using parameters based on the area or size of the circle projected by the particle, the variation in laser thickness alone can lead to non-negligible errors.

Note that the proposed model treats mono-dispersed particles. For a polydispersed system where the particle size varies, assuming the particle size distribution (PSD) function is $f_\mathrm{p}(r)$, the CDF of the polydispersed system can be weighted-averaged according to the PSD as $F(r) =$

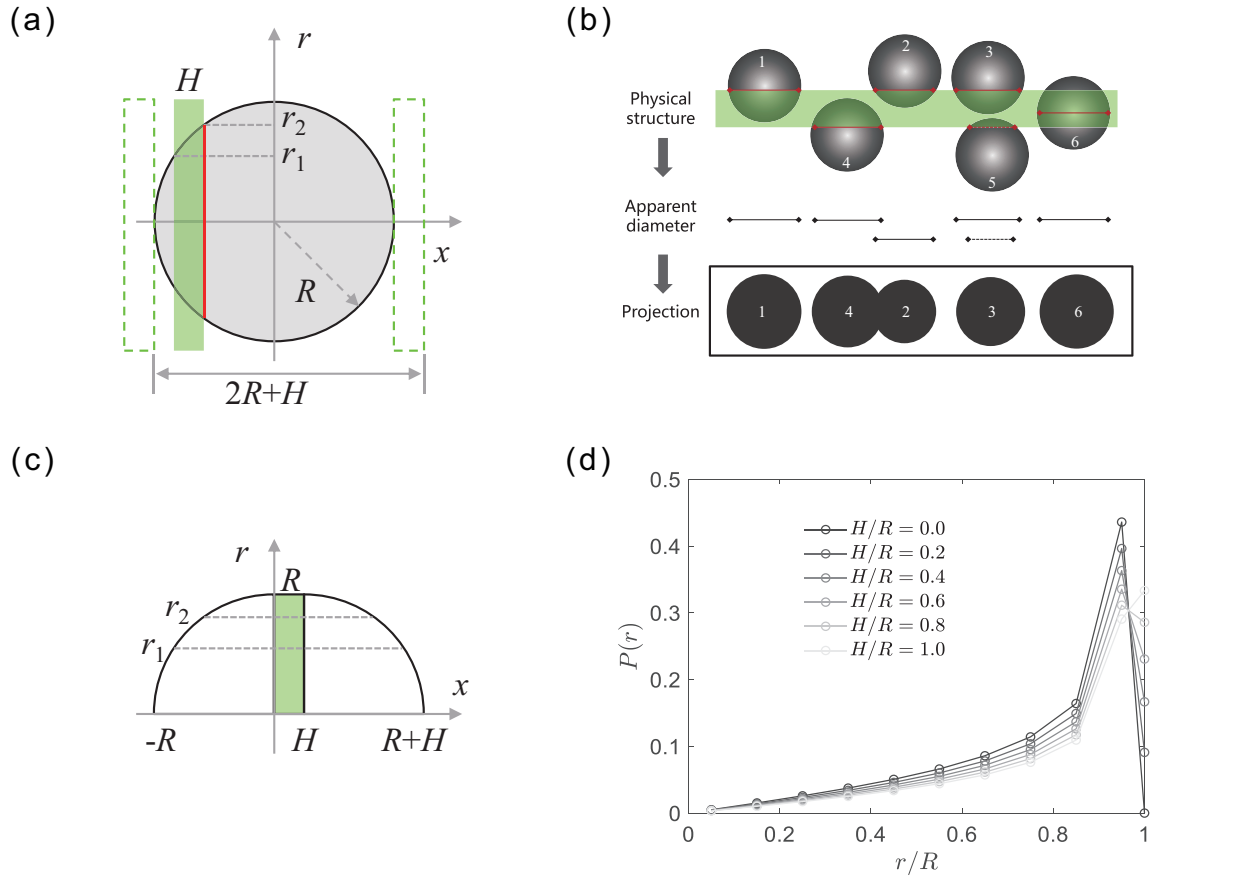

Figure 1 (a) Ideal projection procedure in the RIM experiment. (b) Projection of a particle system. The red lines represent the apparent diameters. Particle 5 is undetected owing to the overlapped projection with particle 3. (c) Relationship between the apparent radius r and the position of the laser relative to the particle center, x. (d) Occurrence probability of r. The horizontal coordinates of the data points are the median values of an interval with width $0.1R$, i.e., $P_{k+1/2} = P[0.1(k-1) \le r/R < 0.1k], k = 1, 2, \cdots, 10$, and $P(r/R = 1) = H/(2R + H)$.

$\int_0^r f_p(r')F(r')\mathrm{d}r'$. Note also that there is not much essential difference between this projection model and that used in stereology [37-39]. However, the proposed apparent size distribution model is simpler in form and explicitly describes the influence of the laser thickness.

2.2.2 *Laser intensity and image brightness*

In fluid experiments, the concentration of the fluorescent dye, C, is typically treated as a passively transported scalar to study its structure in space and time [40]. As a direct representation of the fluorescence intensity, the image brightness is often used to recognize the dye concentration. However, the dye concentration in the fluid is usually uniform in an RIM experiment, which is a typical particle-liquid flow. What actually affects the local fluorescence intensity F is the local content of the solid phase described by the volume fraction ϕ. In a weak excitation system [40], $F \propto IC(1-\phi)$, where the local laser intensity I varies according to the Bouguer-Lambert-Beer law:

$$\frac{\mathrm{d}I}{I} = -\varepsilon C(1-\phi)\mathrm{d}r. \tag{5}$$

Solving this ordinary differential equation gives the laser intensity

$$I(r) = I(r_0)\exp\left[-\varepsilon\int_{r_0}^{r} C\,(1-\phi)\,\mathrm{d}r'\right]. \tag{6}$$

Besides, for a radial laser sheet, it is necessary to introduce another brightness variation factor to the equation that takes into account the laser divergence given by $f(r) = r_0/r$. It is thus evident that the laser intensity is related to the investigated position and the lighting history along the laser path. Therefore, directly using image brightness to represent volume fraction is usually inadvisable, and a modification based on the laser intensity attenuation is needed at least [41]. A more comprehensive approach requires a rigorous calibration and calculation system based on the PLIF technique, which is somewhat troublesome.

Therefore, this study does not use image brightness to determine the solid volume fraction, and mainly uses the geometric information including the particle location and size as will be seen below.

3. Calibration experiment and analysis method

To find the image indicators that are best related to the volume fraction, it is necessary to perform calibration experiments by creating particle-liquid mixtures with different ϕ values. A simple way is to use a RI and density matching system where the particles are ideally neutrally buoyant and suspended in the fluid, so that the packing can remain relatively stable for a certain time and be used for picturing and analysis.

3.1 Experimental setup

The solid phase is chosen to be polymethyl methacrylate (PMMA) particles. As shown in Fig. 2, the PSD generally follows a log-normal distribution with mean diameter $D \approx 3.77$ mm, polydispersity $\delta = \sqrt{\langle \Delta R^2 \rangle}/\langle R \rangle \approx 0.0102$ and skewness $S = \left\langle \Delta R^3 \right\rangle / \left\langle \Delta R^2 \right\rangle^{3/2} \approx 0.0306$. The granular density is 1180 kg/m^3 and the RI is approximately 1.490. The RI and density matched fluid is a mixture of ammonium thiocyanate, glycerin and water with weight proportions of 39.23%, 36.17%, and 24.60%, respectively [42]. The fluorescent dye rhodamine 6G is also added to enhance contrast between the solid and fluid phases.

The mixture is held in a PMMA box with a size of $6\times15\times10$ cm^3 as shown in Fig. 3(a). A glass rod with diameter $D_{\text{rod}} \approx 4$ mm is used to stir the mixture so that the particles reach a suspended state. Though a fluidization cell can be used for more uniform and stable packing samples [22], the much simple stirring method is adopted here considering the fact that the particles are approximately neutrally buoyant. Furthermore, the rectangular geometry, the vertically stratified flow behavior and the layered-statistical manner are almost the same as those of the widely investigated inclined flow, which is an application of this study that will be presented in Sect. 5.

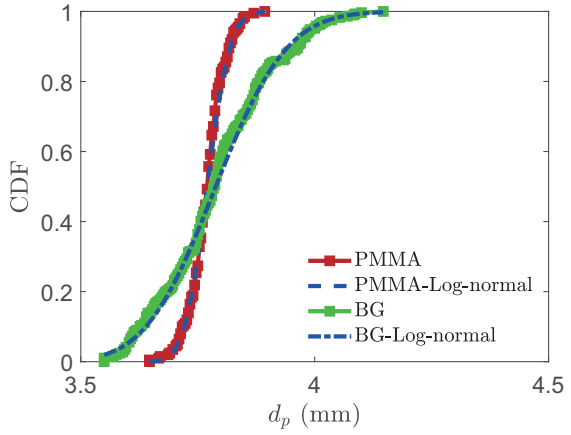

Figure 2 By-number particle size distributions of the PMMA particles used for the calibration experiments, and borosilicate glass used for the inclined flow experiments. The dashed and dash-dotted lines are the corresponding log-normal fittings.

A green laser beam (527 nm) is produced by a pulse laser generator (Vlite-Hi-10K, Beamtech Optronics Co., Ltd.) that is reshaped into a transversely uniform laser sheet by a Powell lens. The laser sheet thickness varies from 1.0 to 1.5 mm in the ROI. Note that the thickness is from the measurement of the width of the laser illumination on a paper under safe laser intensity, which is a rough estimation of the laser sheet thickness and for reference only. Actually, there is no consensus on how to measure the laser sheet thickness. The definition based on the standard deviation of the Gaussian profile may be more representative [43-45], but is not further discussed here.

Different values of the bulk solid volume fraction Φ are obtained by mixing different amounts of particles and liquid. In practice, the sample with lower Φ is prepared first, after which a certain amount of liquid is continuously sucked out and Φ is recalculated. Therefore, higher Φ generally has lower heights. A total of 19 samples are prepared with Φ covering 0.17-0.62. The height varies in the range 9-15D as shown in Fig. 4(a). The intrusion of the glass rod will induce volume fraction deviation from the designed value of $\pi D_{\text{rod}}^2/4LW \approx 0.0014$, which is less than 1% for $\Phi > 0.17$ investigated in this study and is thus negligible.

3.2 Image processing

The raw images are first adjusted by the contrast-limited adaptive histogram equalization (CLAHE) to enhance contrast and equalize the brightness resulting from the laser intensity variation. A circle recognition algorithm based on the circular Hough transform is then adopted [46, 47]. Almost no circle is observed with an apparent radius less than $0.5R$, so the lower bound for the circle recognition algorithm is set as $0.5R$. For the recognized k-th circle with apparent radius r_k centered at (x_k, z_k), the covering pixels are $I_{ij}^k \in \left\{(X_i, Z_j) | (X_i - x_k)^2 + (Z_j - z_k)^2 < r_k^2\right\}$. In case that the averaged value $\bar{I}_{ij}^k > 0.5 I_k^*$ or the median value $\text{mid}\left\{I_{ij}^k\right\} > 0.3 I_k^*$, the circle is seen as misrecognized and then rejected. The former condition is used to reject those circles with higher brightness mainly due to setting an improperly high sensitivity for the algorithm, and the latter for

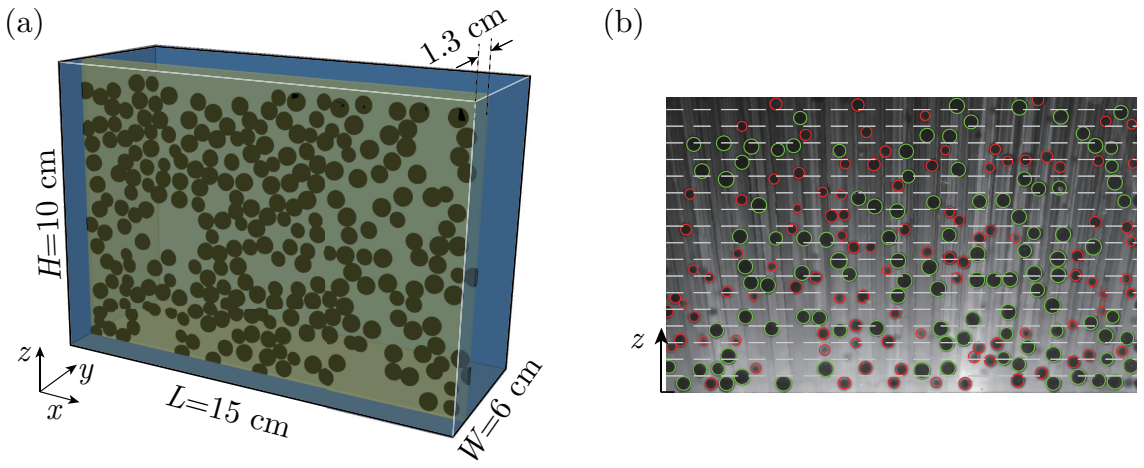

Figure 3 (a) Sketch of the experimental setup. (b) Typical circle recognition result with $\Phi = 0.17$. The green and red circles have apparent radii $r > 0.8R$ and $r < 0.8R$, respectively. The horizontal dashed lines represent the boundaries of the statistical bins.

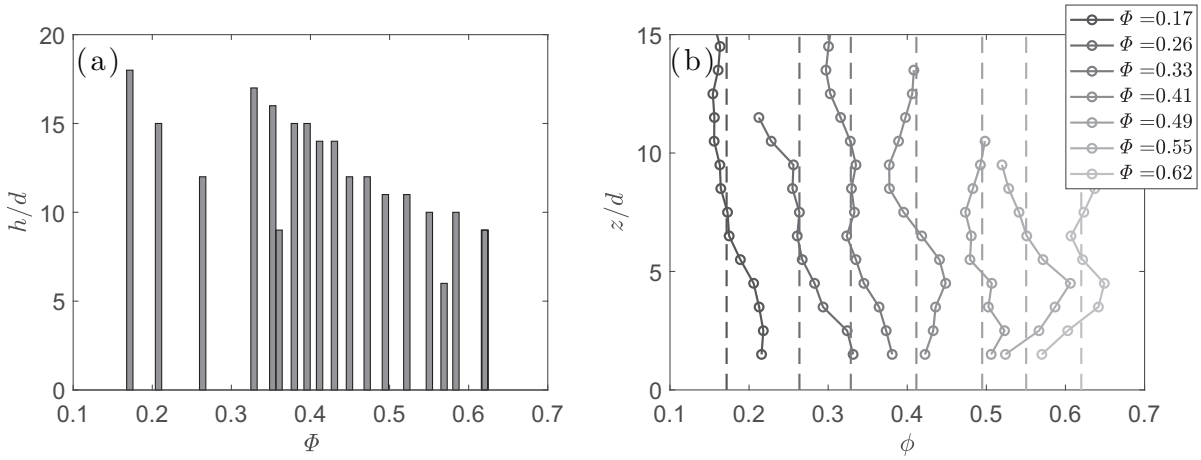

Figure 4 (a) Bulk solid volume fraction Φ and corresponding effective packing height h of the designed cases. (b) Typical results for local volume fraction after modification. The dashed lines are the corresponding bulk volume fractions.

misrecognition near the stripes. The characteristic brightness is $I_k^* = \max(1, r_k/R)$, which considers the fact that particles deviating from the laser sheet typically have higher imaging brightness owing to the contribution of the fluid fluorescence aside. In addition, owing to the small interparticle distance especially in dense packing, occasionally overlapped circles emerge owing to the image misrecognition. An overlap detection method is therefore introduced to reject these circles. The basic idea is to reject the circles whose overlapping areas with other particles are larger than 0.5 times their own areas. The recognized circles are sorted according to the apparent size and the smaller ones are judged in priority. The circle satisfying the criterion is rejected and no longer considered when larger particles are detecting the overlapping area. The parameter 0.5 is an empirical value. For the experimentally recognized circles, such a large overlap area is not usually achieved unless misrecognition happens.

Figure 3(b) shows a typical result with the finally obtained circles using the above circle recognition algorithm and the method for rejecting misrecognized circles. We have occasionally examined the performance of the image processing method and found good robustness.

3.3 Statistical methods

This study adopts the layered-statistical method, which is widely used in unidirectional and uniform flows where all information at the same elevation is assumed to be identical [9, 10]. The statistical bins are arranged from the bottom of the ROI with each having a height of $1D$ as shown in Fig. 3(b). Each recognized circle is assigned to the corresponding bin according to its vertical coordinate z. The geometric parameters related to circles in the same bin are averaged. To avoid boundary effects, the data of the first near-wall and near-free-surface layers are neglected. The horizontal size of the ROI is approximately $40D$, and typically more than 1000

frames are used for statistics to ensure more than 10000 data for each bin, which is thought to be large enough for meaningful statistical results [22].

In practice, the PMMA particle density is found to vary even for the same batch, so a strict suspension is hardly obtained, and the particles could settle and distribute non-uniformly in height. This results in deviation of the local volume fractions ϕ from the bulk volume fraction Φ. Considering the solid mass conservation, Φ is related to ϕ as

$$\Phi = \int_0^h \phi \mathrm{d}z/h. \tag{7}$$

This study eliminates this settling effect by modifying the bulk volume fraction Φ into local volume fractions ϕ_m of m-th bin ($m = 1, 2, \cdots, M$) based on the particle number n_m assigned to this bin as

$$\frac{\phi_m}{\Phi} = \frac{n_m}{\sum_{m=1}^{M} n_m/M} \tag{8}$$

with M being the total number of bins. The modified local volume fractions ϕ_m are treated as the true ϕ in the following. Figure 4(b) shows the modified local volume fraction, which tends to be low at greater height and high at lower height, indicating the settling effects. However, the deviation of ϕ from Φ is generally within ±0.05. Note that this modification is a posteriori and somewhat reduces the reliability of the actual solid volume fraction. The possible change in the number of observed particles due to laser sheet distortion is also omitted. Appendix gives the calibration results based on the bulk volume fraction. It will be seen that though the data errors widen, the conclusions obtained from this study are basically not affected.

When relating the indicators with the volume fraction, the accuracy of the models is judged from three aspects. First, the coefficient of determination, R^2, which describes how well the observed data is replicated by the model. Second, the root mean squared error (RMSE), which is a systematic measurement of the differences between the model prediction and the observed data. Third, the relative deviation of the observed data points from the model prediction compared with the ±10% and ±20% error bounds, which reflects the maximum error that might be induced by the indicators.

4. Results and discussion

4.1 Apparent size distribution

As mentioned before, the laser sheet is distorted after passing the transparent soil. Section 2.2.1 also shows that the variation in laser sheet thickness will influence the apparent size of the projecting particles. This section examines the experimentally observed apparent size distribution at different elevations.

Figure 5(a) shows the experimental result and the theoretical prediction. The theoretical prediction given by the dashed line increases almost monotonically. However, the experimental result is different from the theory in that the apparent size probability distribution $P(r)$ shows a bimodal distribution peaking at $r \approx 0.62R$ and $r \approx 0.97R$. This bimodal distribution exists in all cases though the exact curves might differ. Note that Fig. 5(a) gives the result for $\Phi = 0.17$, where there is almost no obvious interparticle contact as evidenced in Fig. 3(b), indicating that the bimodal distribution is not likely a result of particle interactions. A possible explanation is that refraction occurs at the particle-fluid interfaces owing to RI mismatch. As a result, the actual illuminated portion of the particles is larger than expected, which leads to larger apparent size. The refraction is more effective for particles leaving the laser sheet, which have larger angles of incidence, contributing to the probability peak at $r \approx 0.62R$. This hypothesis also helps explain why almost no circles appear with $r < 0.5R$.

Further observation of the apparent size distribution at different elevations reveals that the peaks shift leftward with increasing height, implying that more particles are projecting circles with smaller apparent sizes. The curves also show increasing smoothness and the decreasing peak values. This reflects the increasing distortion of the laser sheet with deeper penetration, which introduces random and unexpected off-laser-sheet information. The laser sheet distortion cannot be simply treated as increased beam thickness because the number of smaller circles actually increases in contrast to the prediction by the theoretical model given by Eq. (1) that the probability for full-sized projection increases with increasing laser thickness.

The aforementioned phenomena are related to the projection and imaging procedure, and the image processing method may also play a role. Specific causes are beyond the scope of this study and may warrant other focused research. Nevertheless, the experimental results show that the apparent circle size correlates with height.

The corresponding averaged circle area for each elevation is shown in Fig. 5(b). Significant fluctuation is observed with relative differences up to 10%. Note that the fluctuation is not a result of the layered packing structure with a characteristic length of one particle diameter D, see for example those reported by Allen and Kudrolli [48] and Ni and Capart [49]. The statistical bin has a height of D, which already covers the fluctuating length. It is thus predictable that indicators based on the apparent size or area of the recognized circles, such as the area fraction, will be severely affected by noise

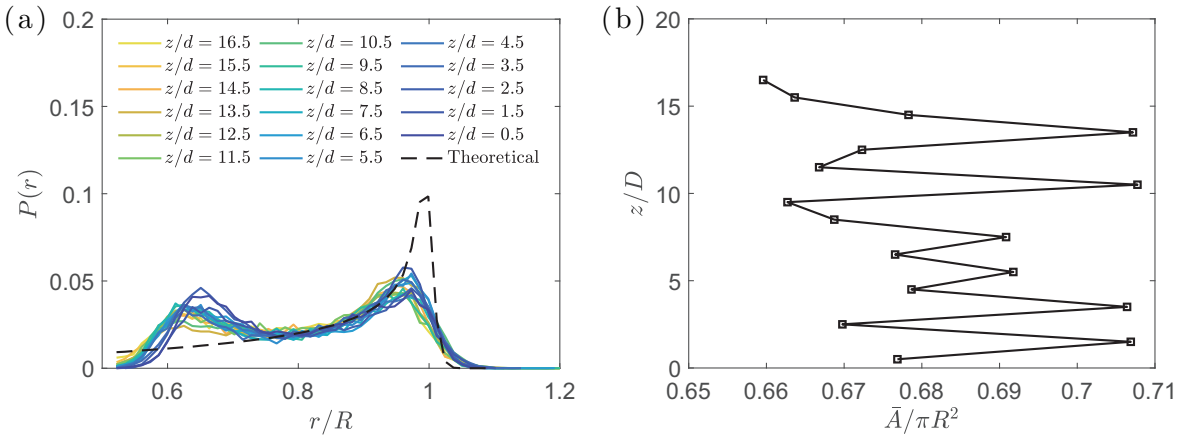

Figure 5 (a) Probability distribution of apparent size at different elevations for $\Phi = 0.17$. The theoretical result has considered the physical particle size distribution for $H = 0$. (b) Variation in averaged area of the recognized circles in each statistical bin.

and show high uncertainty. This factor is basic and important but has never been paid attention to in the past studies.

4.2 Area fraction

The area fraction c_{2D} is the most widely used indicator of the solid volume fraction especially in RIM systems [26, 48]. It is defined as the area proportion of the solid phase in a representative area element. Proper image processing methods such as binarization or characteristic profile recognition as adopted in this study are needed to obtain a credible solid phase area. In this study, the area of each recognized circle is assigned to a bin and its neighboring bins according to their geometric relationship if they intersect. The area fraction is clearly defined in a 2D form, and proper conversion to the 3D volume fraction is needed.

Figure 6 gives the relationship between the area fraction and volume fraction c_{2D}-ϕ, where each point comes from the statistical result of one bin. Because the image properties may be related to position, the points are colored according to their height from the ROI bottom, z/d, similarly to Fig. 5(a). It is observed that the brighter points tend to move downward compared to their neighbors, indicating that the area fraction tends to decrease at higher elevation even after the volume fraction is modified. This phenomenon is related to the apparent size variation at different elevations presented in Sect. 4.1.

Following previous investigations based on the RIM technique, ϕ is assumed to be a proportional function of c_{2D}, i.e., $\phi = ac_{2D}$, where a is the proportionality coefficient determined from calibration based on the result at $\phi_0 \approx 0.58$. Figure 6(a) shows that the proportional function is difficult to fit to the data and may induce significant error for $\phi \leq 0.4$, which is away from the calibration point. In fact, the c_{2D}-ϕ

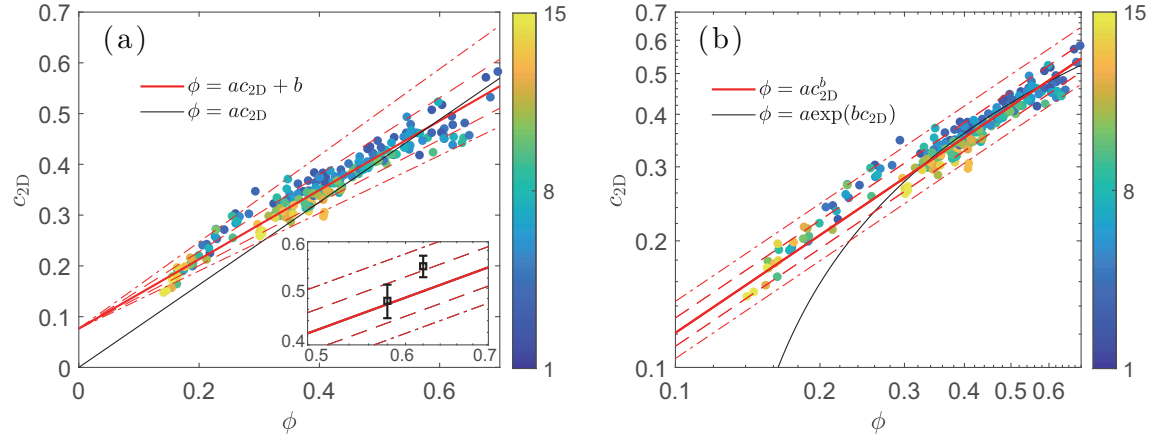

Figure 6 Relationship between the area fraction c_{2D} and volume fraction ϕ on (a) linear plot and (b) log-log plot. The color of the points defined by the color bar represents the height from the ROI bottom. The dashed and dash-dotted lines represent the $\pm 10\%$ and $\pm 20\%$ error bounds, respectively (same as following). The inset in (b) gives the calibration results for the borosilicate glass particles, details of which are given in Sect. 5.

relationship is observed to be a shifted linear function:

$$\phi = ac_{2D} + b \tag{9}$$

with the parameters given in Table 1, which greatly improves the agreement between the model and the observed results. Note that the coefficients a and b used in this paper are usually generic and do not correspond to each other unless otherwise stated. The linear model can also be written as $\phi = 1.466\,(c_{2D} - 0.0765)$, implying that a non-negligible intercept needs to be subtracted from the area fraction so that the traditionally adopted proportional function holds. However, the error bounds in Fig. 6(a) show that at median volume fraction $\phi \approx$ 0.3-0.4, the observed results deviate more than 10% from the linear model and even more than 20% at more dilute state. Note that the laser sheet thickness is non-negligible compared to the particle size with $H/R \in [0.5, 0.8]$ and the intercept is likely to be related to the overprojection effect. As can be expected, the larger the laser thickness is, the larger the apparent size is and the smaller the intercept (larger absolute value) is. The proportionality may still hold with an ideal infinitely thin and undistorted laser sheet considering the Delesse principle [50].

In the log-log plot, Fig. 6(b) shows that the power-law function:

$$\phi = ac_{2D}{}^{b} \tag{10}$$

also performs well, though a deviation up to 20% is also observed. Note that although the power-law and linear models have similar R^2 and RSME values given in Table 1, the former is more reasonable because in the dilute regime when $c_{2D} \to 0$, the power-law function $\phi = ac_{2D}{}^{b} \to 0$ while the linear function $\phi = ac_{2D} + b \to b$. If more dilute packing is investigated, the power-law model is likely to be more appropriate. The results reported in this paper have already shown an improvement for $\phi \approx 0.17$, but there is no much difference between the two models for larger ϕ.

The exponential model $\phi = a\exp^{bc_{2D}}$ proposed by Sarno et al. [26] is also examined here. The observed results deviate significantly from this model when $\phi < 0.3$. This is probably due to the fact that Sarno et al. [26] focused on the near-wall volume fraction and the area fraction was obtained from binarization to recognize particle surfaces illuminated by a particularly aligned light source. Their image processing and data acquisition both differ from those of the present study, leading to the difference between the prediction models.

In summary, this section has compared four c_{2D}-based predictive models: the proportional, linear, power, and exponential functions. The traditionally adopted proportional model is found to be inapplicable to the present result and to have significant error in predicting the volume fraction away from the calibration point. The exponential model is only applicable to higher volume fraction in the range $\phi \geq 0.3$. The linear and power-law models satisfactorily describe the c_{2D}-ϕ relationship under the whole range of volume fractions, Φ = 0.17-0.62, studied in the paper, though deviations of more than 10% or even 20% between the observed data and the models are found for $\phi < 0.3$. This is mainly due to the noise from the laser distortion and variation in the apparent size, which may play more essential roles under low packing density. It should be noted that a flow state with $\phi < 0.3$ also appears fluently in granular flow such as the near-surface transport layer in sediment transport [51, 52]. Therefore, there is still a need to develop volume fraction models that are more accurate and less affected by apparent size variation.

Table 1 Solid volume fraction prediction models and the corresponding parameters

Indicators	Models	Fitting parameters		R^2	RMSE
		a	b		
c_{2D}	$\phi = ac_{2D}$	0.8140	–	0.86	0.049
	$\phi = ac_{2D} + b$	1.466	−0.1121	**0.93**	**0.034**
	$\phi = a\exp(bc_{2D})$	0.1162	3.428	0.89	0.043
	$\phi = ac_{2D}^{b}$	1.546	1.296	**0.93**	**0.034**
ξ_i	$\frac{\phi}{\phi_{rcp}} = \left(\frac{\xi_i - \xi_{min}}{a - \xi_{min}}\right)^b$	0.8705	0.8311	0.89	0.062
d_{poly}	$\frac{\phi}{\phi_{rcp}} = \frac{1}{\left(ad_{poly}/D\right)^b}$	0.9416	2.663	**0.97**	**0.035**

4.3 Indicators based on the Voronoi diagram

If the center of each recognized circle is seen as a generator $\boldsymbol{p}_i = (x_i, z_i)$ $(i = 1, 2, \cdots, n)$, a Voronoi diagram (VD) is a partition of the image plane in which the points in each Voronoi cell P_i are closer to its generator $\boldsymbol{p}_i$ than to any other generators [53]. Generally speaking, the Voronoi diagram (VD) is a space partition method widely used in mathematics, but has become a powerful tool in many other areas including the granular materials. A typical 2D VD is shown in Fig. 7, where each VD cell is a polygon. Following its definition, the VD actually provides a local space related to a particle and hence more information can be derived from the discrete system, such as the local porosity and strain [54, 55].

4.3.1 Voronoi roundness

Based on the geometric properties of the 2D VD, Capart et al. [22] proposed a pattern-based method for determining the near-wall volume fraction which related the volume fraction to the roundness of the cells via

$$\frac{\phi}{\phi_{rcp}} = \left(\frac{\xi_i - \xi_{min}}{\xi_{rcp} - \xi_{min}}\right)^b. \tag{11}$$

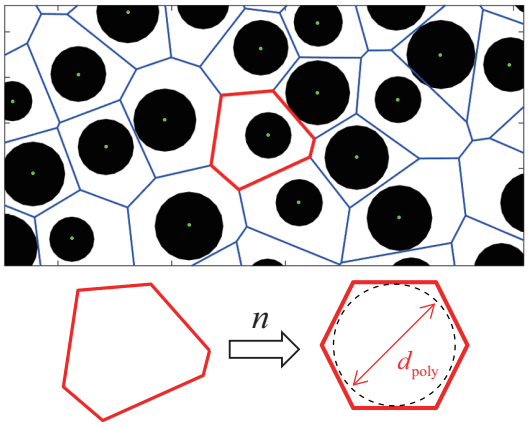

Figure 7 Typical 2D Voronoi diagram shown as blue polygons with $\Phi = 0.38$. The green dots are the centers of the black recognized circles and are also the generators of the VD. Below shows an n-sided regular polygon with an inscribed circle of diameter d_{poly}, which is area equivalent to a typical n-sided Voronoi cell.

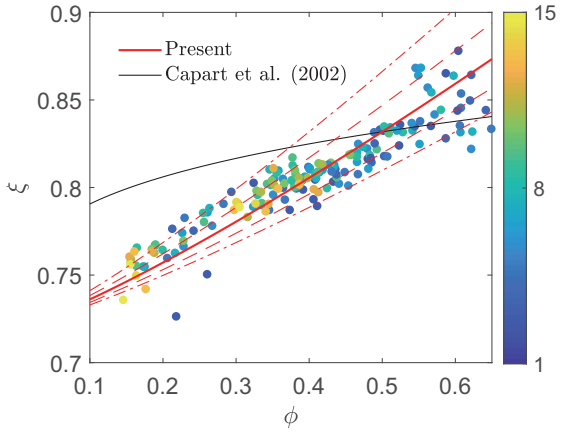

Figure 8 Relationship between the roundness of the Voronoi cells and the volume fraction. The solid lines represent Eq. (11).

Here, the roundness of cell P_i is defined as $\xi_i = 4\pi A(P_i)/L(P_i)^2$, where $A(P_i)$ and $L(P_i)$ are the area and perimeter of the cell, respectively. ϕ_{rcp} and ξ_{rcp} in Eq. (11) are the volume fraction and roundness of random close packing (RCP), respectively. ξ_{min} is the minimum roundness when the volume fraction tends to zero. b is a model parameter. Capart et al. [22] obtained $\xi_{min} = 0.72$ from Monte-Carlo simulation and further fitted the parameters as $\xi_{rcp} = 0.84$ and $b = 3.5$ through a fluidization cell test. Desmond and Weeks [56] systematically investigated the influence of the PSD on the RCP density ϕ_{rcp} and proposed the empirical formula $\phi_{rcp} = 0.634 + 0.0658\delta + 0.0857S\,\delta^2$. The PSD of the PMMA particles used in this study reaches a packing density $\phi_{rcp} = 0.6347$. It is seen that the size polydispersity and skewness do not have much influence on the packing density, and the granular system is close to the monodisperse system where $\phi^0_{rcp} = 0.634$.

The roundnesses ξ_i of the cells whose generators are located in the same statistical bin are averaged (see Sect. 3.3). The relationship between the averaged roundness and the volume fraction ξ-ϕ is shown in Fig. 8. The result from Capart et al. [22] is seen differing significantly from the observed results. This sheds light on the differences between near-wall particle locations and the internals obtained from the RIM experiments. The near-wall particles are laterally confined by the side wall, which requires the particles to remain on only one side of the wall, and the lateral positions (y) are approximately equal for a monodisperse system, i.e., one dimension is fixed. In contrast, the particles observed in the RIM experiment exist on both sides of the laser sheet, and the lateral positions are random. As a result, the volume fraction determination models are not likely to be same for the ones based on near-wall and inner image indicators.

Nevertheless, Eq. (11) and $\xi_{min} = 0.72$ are still adopted and the other parameters are fitted, leading to $\xi_{rcp} = 0.87$ and $b \approx 0.83$ as given in Table 1 and shown in Fig. 8. Though the fitted formula agrees qualitatively with the experimental result, a deviation up to 20% is observed in the whole investigated volume fraction. The R^2 and RSME values in Table 1 show that the predictive model based on roundness is less accurate than the linear or power-law model based on the area fraction.

4.3.2 *Equivalent diameter*

Considering the definition of the VD, a 3D VD cell, which is a polyhedron, can be seen as the local free space for a generator-associated particle. The local volume fraction ϕ_{local} can be defined as the ratio of the particle volume V_p to the cell volume V_{P_i}, i.e., $\phi_{local} = V_p/V_{P_i}$ [54, 57]. The idea can be introduced to the 2D case. However, the 2D cells are not directly from a section of 3D cells, but are regenerated from the projected centers of the particles that intersect the laser sheet. Therefore, a quantitative correlation between the sizes of the 3D and 2D cells is not readily obtained.

To measure the size of a typical n-sided 2D Voronoi cell, this study introduces the diameter d_{poly} of the inscribed circle of an n-sided regular polygon, which is area equivalent to the cell. In the following, d_{poly} is referred to as the equivalent diameter. From the geometric relationship, one has $d_{poly} = 2\sqrt{A(P_i)/(n\tan\pi/n)}$. d_{poly} actually represents the center distance between the neighboring particles sharing the same cell edge, especially in the dense packing state where the particles are orderly arranged.

In the RCP state, neighboring particles are in close contact with each other, and the interparticle distance may be approximately D. Then, for a packing with average interpar-

ticle distance d_{3D}, the volume fraction is

$$\frac{\phi}{\phi_{rcp}} = \frac{V_p/d_{3D}^3}{V_p/D^3} = \frac{1}{(d_{3D}/D)^3}. \tag{12}$$

The question is how d_{poly} obtained from the 2D images is related to d_{3D}. Liu et al. [58] theoretically derived a power-law relationship between the interparticle distance and the packing parameters mainly including the particle size and packing density under different dimensions. Based on this theoretical work, this study assumes the relationship between d_{poly} and d_{3D} to be

$$\frac{d_{3D}}{D} = \alpha\left(\frac{d_{poly}}{D}\right)^{\beta}. \tag{13}$$

The parameters α and β should include the effect of the physical PSD, apparent size distribution, dimensional number, particle spatial distribution, and c_{2D}-ϕ relationship. Theoretical expressions are difficult to obtain, if not impossible, so this paper relies on data fitting to obtain its numerical results. Substituting Eq. (13) into Eq. (12) yields

$$\frac{\phi}{\phi_{rcp}} = \frac{1}{\left(ad_{poly}/D\right)^b} \tag{14}$$

with $a = \alpha^{1/\beta}$ and $b = 3\beta$.

The equivalent diameters of the cells whose generators are located in the same statistical bin are averaged to obtain d_{poly} for the bin. The relationship between d_{poly} and the volume fraction d_{poly}-ϕ is given in Fig. 9. Despite several outliers, the data are well contained in the ±10% error bound. The fitting parameters are given in Table 1. It is seen that the model based on d_{poly} gives the best description of the observed results. From the construction stage, it is seen that the VD is only related to the position of the recognized circles and not affected by the apparent size or imaging brightness. As a result, the d_{poly}-based model is less affected by the variation in observation conditions such as RI mismatch or laser intensity. This feature reduces the requirement for consistency between the calibration experiments and the actual measuring experiments, which considerably improves the applicability and flexibility of the proposed model.

However, it should be noted that the fitting parameters are not readily applied to other experiments. Because the VD is a partition of the space, the size of each cell is inversely proportional to the number of recognized circles. Therefore, different values of the laser thickness H/D and particle polydispersity may result in different parameter values, which is also the case for the c_{2D}-based models. Furthermore, there are two parameters in the model, and no apparent correlation between them is found for now. Hence, the model parameters need to be properly determined by applying at least two

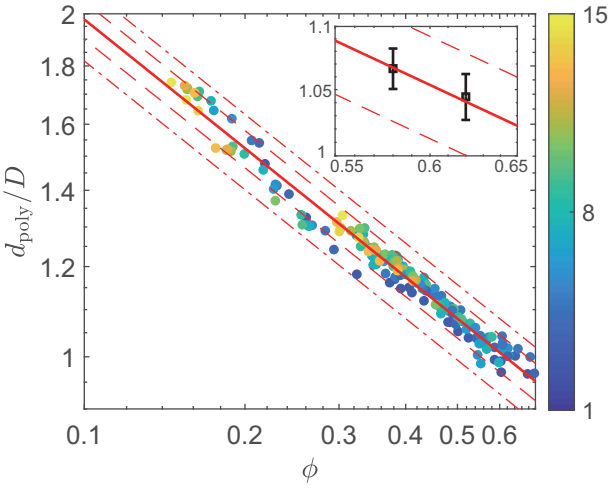

Figure 9 Relationship between the equivalent diameter and volume fraction. The solid lines represent Eq. (14). The inset gives the calibration results for the borosilicate glass particles, details of which are given in Sect. 5.

packing states with as much of a volume fraction difference as possible. Other schemes may be used if a well-controlled loose packing is difficult to obtain when negatively buoyant particles are used. One example is performing *in-situ* calibration experiments based on the RI and density matching technique using substitutive particles with sizes close to those in the experiments, similarly to the way adopted in this paper. Another possible way may be performing proper bulk statistics and comparing the results with the total solid content under various packing states.

5. Application to two-phase granular flow down an inclined plane

To test the applicability and accuracy of the proposed d_{poly}-based model, this section applies it to the real case of granular flow down an inclined plane, which actually motivated this study. The experiment is based on RIM and uses the same laser and imaging system as those in the previous calibration experiments. The borosilicate glass particles are used here with a density $\rho_s = 2178$ kg/m^3. The PSD curve of the particles is given in Fig. 2. The mean diameter is 3.79 mm, which is almost the same as that of the previously used PMMA particles. The two particle system differs in PSD properties. The borosilicate glass particles have higher polydispersity $\delta \approx 0.0279$ and skewness $S \approx 0.0836$. The resulted RCP density is $\phi_{rcp} \approx 0.6358$ [56]. The RI-matched fluid is a DMSO aqueous solution with density $\rho_f = 1095$ kg/m^3 and dynamic viscosity of 2.37 mPa·s. Details of the RIM system are also given by Sun et al. [59].

As shown in Fig. 10(a), the experiments are performed in an inclined channel with a length of 400 cm and width of 20

cm. The channel base is roughed with glued particles that are identical to the flowing ones. The particle-liquid mixture is stored in a silo with a capacity of approximately 170 L. The silo bottom is connected to the channel with an aperture of 4 cm in height. The observation position is 240 cm away from the channel inlet, where the flow is believed to be fully developed and steady. The laser sheet is set 7 cm away from the side wall. The camera captures the inner flow state with a frame rate of 1000 frames per second and resolution of approximately 1536×741 pixels (≈ 32 pixels/D). A movable basal plate of size 6×6 cm^2 was set as a loading plate right behind the observation section. A 0.1-mm-thick silica membrane is applied to connect the loading plate with the surrounding base and prevent liquid leakage. The loading plate is connected to a piezoelectric sensor to measure the normal stress σ_{m} applied to the loading plate by the mixture. Assuming that the flow is unidirectional, uniform and steady, the bottom normal force would be balanced with the normal-to-channel component of the mixture gravity. Thus, the predicted normal force is calculated by integrating the volume fraction as

$$\sigma_{\mathrm{c}} = g\cos\theta\int_0^h [(1-\phi)\rho_{\mathrm{f}} + \phi\rho_{\mathrm{s}}]\mathrm{d}z, \tag{15}$$

where g is the gravitational acceleration, θ is the inclination, and h is the flow height. With Eq. (7), the above equation can be also written as

$$\sigma_{\mathrm{c}} = gh\cos\theta\left[(1-\Phi)\rho_{\mathrm{f}} + \Phi\rho_{\mathrm{s}}\right]. \tag{16}$$

The experiments were performed with inclinations of 5.96° and 12.49°. Only the results for volume fraction and bottom normal stress are reported here.

The volume fraction is determined from the d_{poly}-based model, i.e., Eq. (14). Because this case and the previous calibration experiment have almost the same relative laser sheet thickness H/D, the exponent b in Eq. (14) is believed to be unchanged at $b = 2.663$, while the coefficient a is adjusted according to the imaging results. Different from previous calibration experiments, the suspension state is difficult to achieve because the particles are negatively buoyant, i.e., $\rho_{\mathrm{s}} > \rho_{\mathrm{f}}$. Thus, an RCP state is first used to adjust the coefficient a and obtain $a = 0.975$. Furthermore, at the latter flow stage under inclination $\theta = 5.96°$, the flow ceases and it is assumed that a uniform loose packing has been obtained. This is the loosest state when the particles are able to sustain stresses through long-time contact [1]. From the bottom normal stress measured by the sensor and Eq. (16), the bulk volume fraction is $\Phi \approx 0.58$. The inset of Fig. 9 shows the relationships between d_{poly} and the bulk volume fraction under the two packing states. It is seen that Eq. (14) and the adjusted parameters agree well with the experimental results with a deviation less than 10%. Note also that the calibration experiment and the inclined flow here adopt different observing depths, i.e., 1.3 cm and 7 cm, respectively. The results indicate that the observing depths do not influence the d_{poly}-based model significantly, though slightly adjustment of the parameter a is needed.

A typical flow state under inclination is shown in Fig. 10(b) with its VD and the volume fraction profile predicted by Eq. (14). The flow on high inclination is categorized as a solid bed flow where no freezing particles exist near the bed [9]. Owing to high flow velocity, the bottom particles collide strongly with the basal fixed particles and induce significant velocity fluctuation of the particles and the observed low volume fraction near the bottom. Closer to the surface, the fluctuation decreases owing to frictional and viscous dissipation, and the volume fraction increases. In comparison, the flow under low inclination, $\theta = 5.96°$, is closer to the loose bed flow. As shown in Fig. 10(c), the bottom flow has a nearly uniform volume fraction of 0.6-0.62. Toward the free surface, the decreasing granular pressure reduces the volume fraction. Apparently, the flow structure and particle interaction mechanisms are different for different flow conditions. But the prediction of the d_{poly}-based model is in accordance with our physical interpretation. More details related to the flow mechanism and rheological properties are beyond the scope of this study and remain to be further investigated.

The power-law $c_{2\mathrm{D}}$-ϕ model is also assessed with the parameters obtained earlier. The calibration results are given in the inset of Fig. 6(a) where the RCP state shows a deviation larger than 10%. As shown in Fig. 10(b), for the flow with $\theta = 12.49°$, the results of the $c_{2\mathrm{D}}$-based model differ significantly from the d_{poly}-based model, and even an unphysical volume fraction reaching 0.6877 appears. The $c_{2\mathrm{D}}$-ϕ result has a profile comparable with that of the d_{poly}-ϕ model for $\theta = 5.96°$, but it shows large fluctuation. Thus, it is believed that the results of the d_{poly}-based model are more acceptable.

The models show abnormity in the first layers near the bottom and flow free surface as shown in Fig. 10(c), which is primarily due to poor particle recognition and the VD construction. Despite these boundary defects, the d_{poly}-based model well captures the volume fraction variation in the middle flow area. The boundary defects are removed by extrapolating the inner value.

Figure 10(d) compares the bottom normal stress measured with the sensor, σ_{m}, and that obtained by integrating the volume fraction, σ_{c} in Eq. (15). The predicted values agree well with the measured values with a relative deviation less than 10%. Note that the model parameters are calibrated from two packing states with $\Phi \approx \phi_{\mathrm{rcp}}$ and $\Phi \approx 0.58$, while the prediction gives reasonable results covering $\phi = 0.35$-0.62. In addition, the volume fraction profiles and the flow height

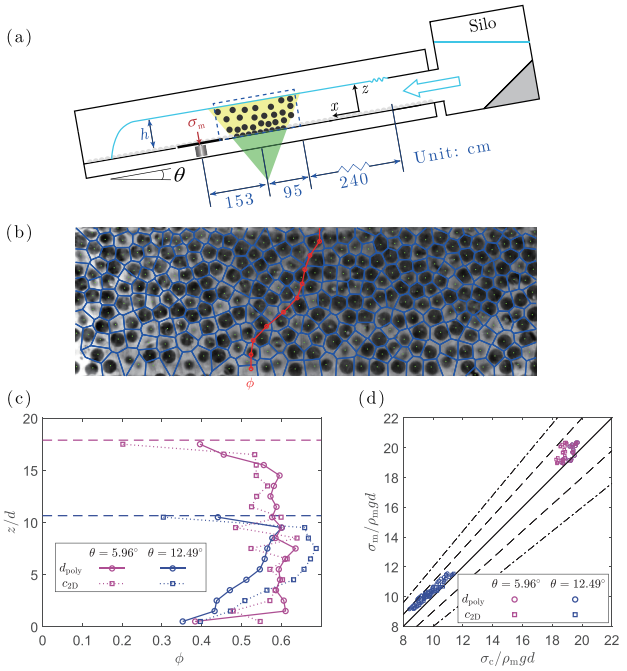

Figure 10 Granular flow down an inclined plane. (a) Sketch of the experiment (not to scale). (b) Typical experimental image with the centers of the recognized circles (green dots) and the VD (blue cells) under inclination $\theta = 12.49°$. The red line shows the profile of the obtained volume fraction. (c) Profiles of the volume fraction under two inclinations. The dashed lines are the flow free surface. (d) Comparison of the bottom normal stress σ_m measured by the sensor and the stress σ_c from integrating the volume fraction.

continuously vary during the flow. Therefore, the d_{poly}-based model shows relatively good accuracy and stability.

6. Conclusions

Despite its wide usage in investigating particle-liquid flow, the RIM technique has long suffered from uncertainties in reconstructing the solid volume fraction ϕ. This study focuses on reasonable imaging methods of measuring ϕ in RIM experiments. The characteristics of the apparent size distribution are theoretically studied, paying particular attention to the influence of the laser sheet thickness. Calibration experiments are performed with the bulk solid volume fraction range 0.17-0.62, and the main findings are three-fold. First, the apparent size distribution varies with elevation owing to laser distortion resulting from RI mismatching. Second, the widely adopted proportional relationship between the area fraction c_{2D} and ϕ results in a large error for ϕ away from the calibration points in cases where the laser sheet thickness cannot be neglected. The linear and power-law c_{2D}-ϕ models are more reasonable but still deviate up to 20% from the experimental results for $\phi < 0.3$. Third, the newly proposed model based on the equivalent diameter d_{poly} of the Voronoi cells is more accurate with a relative deviation generally less than 10% for the whole range of ϕ. The advantage of the d_{poly}-based model lies in its independence of the apparent size, which may introduce noise from the laser sheet distortion. The d_{poly}-based model is applied to study the volume fraction profile and bottom normal force of granular flow down an inclined plane, showing its stability and accuracy.

It should be noted that the model parameters obtained in this paper are not universal. The model parameters need to be calibrated for specific experiments. The variations in parameters with different laser sheet thicknesses and possibly observing depths are reserved for future investigation. Furthermore, this study focuses on granular material that is monodispersed or has a low polydispersity $\delta \leq 0.0279$. The applicability of the present conclusions to systems with higher polydispersity needs to be tested.

Appendix. Results based on the bulk solid volume fraction

The relationships between the imaging indicators and the volume fraction presented in the main text are based on the modified local ϕ described in Sect. 3.3. It should be admitted that this approach reduces the reliability of the volume fraction to a certain degree. To compensate for this deficiency, Fig. A1

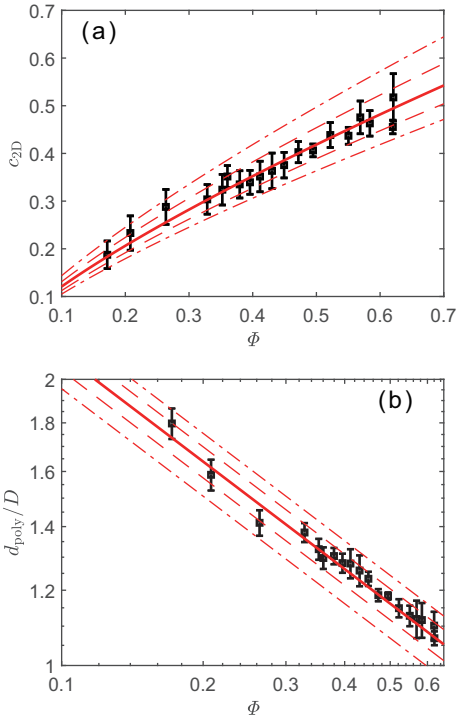

Figure A1 Relationship between the bulk volume fraction Φ and (a) area fraction c_{2D} and (b) Voronoi equivalent diameter d_{poly}. The solid lines represent Eqs. (10) and (14). The model parameters are given in Table 1.

gives the results based on the bulk volume fraction Φ. In this way, the volume fraction is actually considered to be uniform at different elevations, and the indicators vary owing to system error whose standard deviation is given as an error bar. Figure A1 shows that the experimental results still agree well with the model predictions, though the relative error increases. The main conclusions of this paper remain unchanged.

Conflict of interest *On behalf of all authors, the corresponding author states that there is no conflict of interest.*

Author contributions ***Yunhui Sun:*** *Methodology, Investigation and Formal analysis, Writing – original draft.* ***Yi An:*** *Methodology, Writing – review & editing.* ***Jiajun Jiao:*** *Investigation and Formal analysis.* ***Xiaoliang Wang:*** *Writing – review & editing, Funding acquisition and Supervision.* ***Qingquan Liu:*** *Conceptualization, Writing – review & editing, Funding acquisition and Supervision.*

Acknowledgements *This work was supported by the National Natural Science Foundation of China (Grant Nos. 12032005 and 12172057). We also thank Mark R. Kurban for editing a draft of this paper.*

1 B. Andreotti, Y. Forterre, and O. Pouliquen, Granular Media: Between Fluid and Solid (Cambridge University Press, Cambridge, 2013).
2 Y. Forterre, and O. Pouliquen, Flows of dense granular media, Annu. Rev. Fluid Mech. **40**, 1 (2008).
3 A. Armanini, Closure relations for mobile bed debris flows in a wide range of slopes and concentrations, Adv. Water Resources **81**, 75 (2015).
4 A. Armanini, M. Larcher, E. Nucci, and M. Dumbser, Submerged granular channel flows driven by gravity, Adv. Water Resources **63**, 1 (2014).
5 P. Jop, Rheological properties of dense granular flows, Comptes Rendus Physique **16**, 62 (2015), arXiv: 1503.05452.
6 É. Guazzelli, and O. Pouliquen, Rheology of dense granular suspensions, J. Fluid Mech. **852**, P1 (2018).
7 G. Midi, On dense granular flows, Eur. Phys. J. E **14**, 341 (2004), arXiv: cond-mat/0312502.
8 T. Man, P. Zhang, Z. Ge, S. A. Galindo-Torres, and K. M. Hill, Friction-dependent rheology of dry granular systems, Acta Mech. Sin. **39**, 722191 (2023), arXiv: 2205.14898.
9 A. Armanini, H. Capart, L. Fraccarollo, and M. Larcher, Rheological stratification in experimental free-surface flows of granular-liquid mixtures, J. Fluid Mech. **532**, 269 (1999).
10 B. Ferdowsi, C. P. Ortiz, M. Houssais, and D. J. Jerolmack, River-bed armouring as a granular segregation phenomenon, Nat. Commun. **8**, 1363 (2017), arXiv: 1609.06673.
11 P. Aussillous, J. Chauchat, M. Pailha, M. Médale, and É. Guazzelli, Investigation of the mobile granular layer in bedload transport by laminar shearing flows, J. Fluid Mech. **736**, 594 (2013).
12 V. Matoušek, Š. Zrostlík, L. Fraccarollo, A. Prati, and M. Larcher, Internal structure of intense collisional bedload transport, Earth Surf. Process. Landforms **44**, 2285 (2019).
13 L. Rondon, O. Pouliquen, P. Aussillous, Granular collapse in a fluid: Role of the initial volume fraction, Phys. Fluids **23**, 073301 (2011).
14 R. M. Iverson, and D. L. George, A depth-averaged debris-flow model that includes the effects of evolving dilatancy, I. Physical basis, Proc. R. Soc. A. **470**, 20130819 (2014).
15 X. Meng, and Y. Wang, Modeling dynamic flows of grain-fluid mixtures by coupling the mixture theory with a dilatancy law, Acta Mech **229**, 2521 (2018).
16 W. Sun, X. Meng, Y. Wang, S. S. Hsiau, and Z. You, A depth-averaged description of submarine avalanche flows and induced surface waves, JGR Earth Surf. **128**, e2022JF006893 (2023).
17 L. T. Sheng, C. Y. Kuo, Y. C. Tai, and S. S. Hsiau, Indirect measurements of streamwise solid fraction variations of granular flows accelerating down a smooth rectangular chute, Exp. Fluids **51**, 1329 (2011).
18 T. Dyakowski, L. F. C. Jeanmeure, and A. J. Jaworski, Applications of electrical tomography for gas-solids and liquid-solids flows—a review, Powder Tech. **112**, 174 (2000).
19 M. Baur, J. Claussen, S. Gerth, J. Kollmer, T. Shreve, N. Uhlmann, and T. Pöschel, How to measure the volume fraction of granular assemblies using x-ray radiography, Powder Tech. **356**, 439 (2019).
20 Y. Zhao, Q. Bi, Y. Yuan, and H. Lv, Void fraction measurement in steam-water two-phase flow using the gamma ray attenuation under high pressure and high temperature evaporating conditions, Flow Measurement Instrumentation **49**, 18 (2016).
21 T. Revil-Baudard, J. Chauchat, D. Hurther, and P. A. Barraud, Investigation of sheet-flow processes based on novel acoustic high-resolution velocity and concentration measurements, J. Fluid Mech. **767**, 1 (2015).
22 H. Capart, D. L. Young, and Y. Zech, Voronoï imaging methods for the measurement of granular flows, Exp. Fluids **32**, 121 (2002).
23 B. Spinewine, H. Capart, M. Larcher, and Y. Zech, Three-dimensional Voronoï imaging methods for the measurement of near-wall particulate flows, Exp. Fluids **34**, 227 (2003).
24 B. Spinewine, H. Capart, L. Fraccarollo, and M. Larcher, Laser stripe measurements of near-wall solid fraction in channel flows of liquid-granular mixtures, Exp. Fluids **50**, 1507 (2011).
25 P. Dančová, J. Krupička, V. Matoušek, T. Picek, Š. Zrostlík, Validation of laser-penetration- and electrical-conductivity-based methods of concentration measurement in flow with intense transport of coarse sediment, in: EPJ Web of Conferences, 2018. p. 02048.
26 L. Sarno, M. N. Papa, P. Villani, and Y. C. Tai, An optical method for measuring the near-wall volume fraction in granular dispersions, Granular Matter **18**, 80 (2016).
27 J. A. Dijksman, F. Rietz, K. A. Lörincz, M. van Hecke, and W. Losert, Invited article: Refractive index matched scanning of dense granular materials, Rev. Sci. Instruments **83**, 011301 (2012).
28 S. Wiederseiner, N. Andreini, G. Epely-Chauvin, and C. Ancey, Refractive-index and density matching in concentrated particle suspensions: A review, Exp. Fluids **50**, 1183 (2011).
29 S. F. Wright, I. Zadrazil, and C. N. Markides, A review of solid-fluid selection options for optical-based measurements in single-phase liquid, two-phase liquid-liquid and multiphase solid-liquid flows, Exp. Fluids **58**, 108 (2017).
30 F. Blanc, E. Lemaire, A. Meunier, and F. Peters, Microstructure in sheared non-Brownian concentrated suspensions, J. Rheology **57**, 273 (2013).
31 T. Trewhela, and C. Ancey, A conveyor belt experimental setup to study the internal dynamics of granular avalanches, Exp. Fluids **62**, 207 (2021).
32 G. Rousseau, and C. Ancey, Scanning PIV of turbulent flows over and through rough porous beds using refractive index matching, Exp. Fluids **61**, 172 (2020).
33 M. Souzy, H. Lhuissier, Y. Méheust, T. Le Borgne, and B. Metzger, Velocity distributions, dispersion and stretching in three-dimensional porous media, J. Fluid Mech. **891**, A16 (2020).
34 W. Zhang, X. Gu, W. Zhong, Z. Ma, and X. Ding, Review of transparent soil model testing technique for underground construction: Ground visualization and result digitalization, Underground Space **7**, 702 (2022).
35 O. Ciocirlan, and O. Iulian, Density, viscosity and refractive index of the dimethyl sulfoxide + o-xylene system, J. Serb. Chem. Soc. **74**, 317 (2009).
36 V. A. Patil, and J. A. Liburdy, Optical measurement uncertainties due to refractive index mismatch for flow in porous media, Exp. Fluids **53**,

1453 (2012).
37 L. M. Cruz-Orive, Distribution-free estimation of sphere size distributions from slabs showing overprojection and truncation, with a review of previous methods, J. Microsc. **131**, 265 (1983).
38 J. N. Cuzzi, and D. M. Olson, Recovering 3D particle size distributions from 2D sections, Meteorit. Planet Sci. **52**, 532 (2017).
39 D. D. Eisenhour, Determining chondrule size distributions from thin-section measurements, Meteoritics Planet. Sci. **31**, 243 (1996).
40 J. P. Crimaldi, Planar laser induced fluorescence in aqueous flows, Exp. Fluids **44**, 851 (2008).
41 B. Vowinckel, E. Biegert, E. Meiburg, P. Aussillous, and É. Guazzelli, Rheology of mobile sediment beds sheared by viscous, pressure-driven flows, J. Fluid Mech. **921**, A20 (2021), arXiv: 2103.08935.
42 B. C. Bailey, and M. Yoda, An aqueous low-viscosity density- and refractive index-matched suspension system, Exp. Fluids **35**, 1 (2003).
43 A. Borchers, and T. Pieler, Programming pluripotent precursor cells derived from xenopus embryos to generate specific tissues and organs, Genes **1**, 413 (2010).
44 K. Grayson, C. M. de Silva, N. Hutchins, and I. Marusic, Impact of mismatched and misaligned laser light sheet profiles on PIV performance, Exp. Fluids **59**, 2 (2018).
45 M. Shehzad, S. Lawrence, C. Atkinson, J. Soria, A low-cost *in situ* measurement of laser sheet thickness, in: IX Australian Conference on Laser Diagnostics, 2019.
46 T. J. Atherton, and D. J. Kerbyson, Size invariant circle detection, Image Vision Comput. **17**, 795 (1999).
47 H. K. Yuen, J. Princen, J. Illingworth, and J. Kittler, Comparative study of Hough Transform methods for circle finding, Image Vision Comput. **8**, 71 (1990).
48 B. Allen, and A. Kudrolli, Depth resolved granular transport driven by shearing fluid flow, Phys. Rev. Fluids **2**, 024304 (2017).
49 W. Ni, and H. Capart, Stresses and drag in turbulent bed load from refractive index-matched experiments, Geophys. Res. Lett. **45**, 7000 (2018).
50 E. E. Underwood, Stereology, or the quantitative evaluation of microstructures, J. Microsc. **89**, 161 (1969).
51 M. Houssais, C. P. Ortiz, D. J. Durian, and D. J. Jerolmack, Rheology of sediment transported by a laminar flow, Phys. Rev. E **94**, 062609 (2016), arXiv: 1509.08395.
52 R. Maurin, J. Chauchat, and P. Frey, Dense granular flow rheology in turbulent bedload transport, J. Fluid Mech. **804**, 490 (2016), arXiv: 1602.06712.
53 E. A. Lazar, J. Lu, and C. H. Rycroft, Voronoi cell analysis: The shapes of particle systems, Am. J. Phys. **90**, 469 (2022), arXiv: 2201.10842.
54 J. Zhao, and T. Shan, Coupled CFD-DEM simulation of fluid-particle interaction in geomechanics, Powder Tech. **239**, 248 (2013).
55 G. Frenning, A Voronoi strain-based method for granular materials and continua, Comp. Part. Mech. **10**, 427 (2023).
56 K. W. Desmond, and E. R. Weeks, Influence of particle size distribution on random close packing of spheres, Phys. Rev. E **90**, 022204 (2014), arXiv: 1303.4627.
57 A. Amon, P. Born, K. E. Daniels, J. A. Dijksman, K. Huang, D. Parker, M. Schröter, R. Stannarius, and A. Wierschem, Preface: Focus on imaging methods in granular physics, Rev. Sci. Instruments **88**, 051701 (2017), arXiv: 1703.02928.
58 Z. H. Liu, Y. Li, and K. W. Kowk, Mean interparticle distances between hard particles in one to three dimensions, Polymer **42**, 2701 (2001).
59 Y. Sun, W. Zhang, Y. An, Q. Liu, and X. Wang, Experimental investigation of immersed granular collapse in viscous and inertial regimes, Phys. Fluids **33**, 103317 (2021).

基于折射率匹配实验图像指标的含液颗粒物质系统内部固体体积分数重构

孙云辉, 焦佳珺, 安翼, 王晓亮, 刘青泉

摘要 折射率匹配技术被广泛用于研究颗粒-液体混合流动, 但是目前针对其固体体积分数的确定为经验性的且缺乏理论或实验支撑. 为了合理确定内部体积分数, 本文开展了系统的标定实验来研究固体体积分数和图像指标的关系. 结果表明基于面积分数的模型由于颗粒表观尺寸的不稳定性, 会产生较大的误差, 传统使用的正比例模型仅在靠近标定点附近的体积分数成立. 本文提出了基于Voronoi多边形等效直径的预测模型, 结果表明该模型更为准确且稳定, 该模型被进一步应用于颗粒-液体斜槽流动中以研究内部体积分数剖面和底部应力.